

Gate-Tunable Graphene Optical Modulator on Fiber Tip: Design and Demonstration

Zi-xuan Ding, Hao-tian Xu, Yi-feng Xiong, Kang-hu Zhou, Ye Chen, Yan-qing Lu, and Fei Xu*

A fiber-end-face-integrated electrically tunable optical modulator based on graphene field-effect transistor and the fabrication technique are proposed and demonstrated. The all-fiber device features a scheme of compactness and high integration when applied to fiber optical system, as well as a low insertion loss since spatial coupling of light is avoided. A reflecting structure is used and the electro-optic modulator shows vivid modulation when gate voltage gets tuned, with maximum optical reflectance modulation depth over 1% in demonstration. To the best of the authors' knowledge, it is the first time to build an all-solid gate-control modulator directly on fiber facet. The fabrication methods introduce workflows of silicon-on-insulator processing into the optical fiber end-face micromachining domain which can be applied to more comprehensive configurations, broadening the path of fiber-end-face integrated device.

1. Introduction

For long, 2D materials have been gathering concern owing to superb electrical, thermal, mechanical, and chemical properties, including grapheme,^[1] transition metal dichalcogenides (TMDCs),^[2] and black phosphorus (BP),^[3] among which graphene raises in-depth research from analytical theory to experimental application. As a planar atomic-scale carbon crystal with hexagonal lattice, graphene possesses predictable and verifiable light-material-interacting effects such as linear absorption, dispersion, and optical nonlinearity, which enable this functional material to get used in broadband optoelectronic application branches, including photodetectors,^[4] polarizers,^[5] sensors,^[6] and optical modulators.^[7]


Specifically, in the field of light manipulation, the zero-gap Dirac cone structure of energy band and tunable Fermi level make graphene an ideal medium for optical modulation through various approaches, ranging from electrical gating,^[8–11]

thermal controlling,^[12] to all-optical switching.^[13] According to manipulating methods, phase and intensity of light go thorough anticipated change. Routinely graphene can be integrated with waveguide on chip from side to achieve light-matter interaction,^[14–16] which, however, confronts the inevitable coupling loss during connection since the current optical communication systems are comprised of fiber.

Recent decades also see the rapid development of all-fiber-integrated devices. Generally the combinations of functional 2D materials and optical fiber are realized in two methods: side integration and end-face integration.^[17] Side integration uses tapered microfiber^[18] or side-polished D-shape fiber^[19] for evanescent field inter-

action. Particularly, D-shaped fiber provides long-range plane platform for functional material and electrodes integration, which has been applied in advanced fields including controllable optical nonlinearity^[20] and optoelectronic logic gates.^[21] However, this type of integration usually trades insertion loss for modulation depth.^[22] The packaging scale of such device often reaches several centimeters level, hindering further miniaturization. Meanwhile, in certain application fields like fiber laser or fiber Fabry–Perot (FP) cavity,^[23] ultra-compact geometry, moderate-range modulation depth, and fine tunability take up more significance since such systems are sensitive to loss. Therefore, end-face-integrated modulator came into light. Earlier work demonstrated dual-electrode on-facet configuration, where electric current introduced Joule heat and current doping to manipulate graphene's Fermi level.^[12,24] The devices were incorporated in mode-locked ring fiber laser or FP cavity fiber comb for intracavity loss management or wavelength tuning. Nevertheless, dual electrodes provide only one active channel for applying manipulating signals like source-drain current, changing the optical absorption of graphene, fiber facet temperature, or other device parameters simultaneously, which is hard to be decoupled. Besides, the increased local temperature could bring about instability and damage to the device, while the fabrication technique involving mechanical scratching or simple masking lithography also limited the function and performance of graphene. Another solution proposed a kind of reflective gate-controlled graphene device fabricated on silicon wafer,^[25–28] adopting sophisticated microfabrication methods. Light has to be coupled from fiber to space and focused onto

Z.-x. Ding, H.-t. Xu, Y.-f. Xiong, K.-h. Zhou, Y. Chen, Y.-q. Lu, F. Xu
College of Engineering and Applied Sciences
Collaborative Innovation Center of Advanced Microstructures
and National Laboratory of Solid State Microstructures
Nanjing University
Nanjing 210023, China
E-mail: feixu@nju.edu.cn

 The ORCID identification number(s) for the author(s) of this article can be found under <https://doi.org/10.1002/adom.202201724>.

DOI: 10.1002/adom.202201724

wafer-based modulator, then backtracks to fiber after modulation. The complex alignment work in fabrication and application stage undermines the devices' insertion loss and global integration level.

In this work, we report a gate-tunable graphene optical modulator directly fabricated on the tip of optical fiber, which can be summarized as fiber-end-face-integrated graphene field effect transistor mirror (FG-FETM). The method of electron beam lithography (EBL) is introduced into the process of fiber-end-face integration to achieve precise patterning of graphene and microelectrodes, enabling an all-fiber reflecting scheme without spatial coupling loss of light, along with a compact packaging scale to several hundreds of micrometers. The designed structure can function from near- to mid-infrared region owing to the broadband absorption of graphene, while the performance under 1550 nm is specifically demonstrated. Optical reflectance of the device is responsively tuned according to gate voltage, and modulation depth gets changed through employing graphene with varied layer number. It is, to the best of our knowledge, the first time to build an electro-optical transistor directly based on fiber facet.

2. Scheme of FG-FETM

Figure 1a illustrates the schematic diagrams of FG-FETM. Twin electrodes are located symmetrically on the two sides of optical fiber core, bridged by patterned rectangular graphene sheet which covers the core for light-material interaction. Layer of dielectric material is deposited on graphene and

completely covers the graphene sheet, followed with gate electrode on the top of dielectric layer which also plays the role of reflecting mirror. Light input from the fiber core gets reflected in the device, hence interacts with graphene twice. As denoted in side view of Figure 1b, the dual electrodes of gold serve as source and drain, respectively, while the graphene, dielectric (here Al_2O_3 is adopted for processing), and top-gate (reflecting mirror, Cr/Au double layer) constitute a standard parallel-plate capacitor gating model. Here, the dielectric thickness d determines gating efficiency by^[29]

$$E_F = \hbar v_F \sqrt{\pi \frac{\epsilon_r \epsilon_0}{e \cdot d} |V_G + V_0|} \quad (1)$$

where E_F is the Fermi-level, \hbar is the reduced Plank constant, v_F is the Fermi velocity of graphene (here adopted $1.1 \times 10^6 \text{ m s}^{-1}$), ϵ_r is the relative permittivity of dielectric, ϵ_0 is the vacuum permittivity, e is the charge of electron, V_G is the gate voltage, and V_0 is the offset voltage caused by natural doping (here assumed 0). The ideal Fermi-level gate tuning curve of single-layer graphene under 30 and 225 nm Al_2O_3 dielectric is plotted in Figure 1c, demonstrating monotonicity with increasing gate voltage, which lays the foundation for optical modulation. Thinner dielectric layer shows higher Fermi-level tuning efficiency as shown in the plot.

The optical transmittance of graphene can be estimated by^[30–32]

$$T = \left| 1 + \frac{\pi \alpha}{2} \right|^{-2} \quad (2)$$

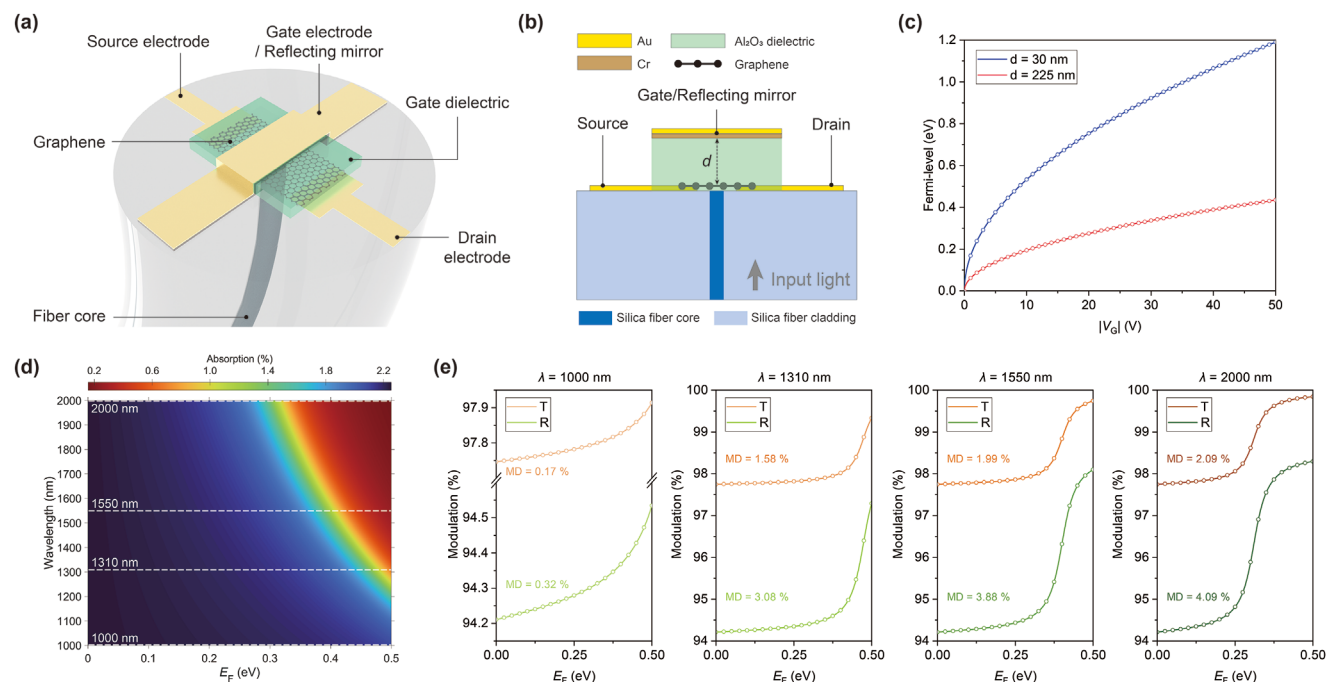


Figure 1. Design of FG-FETM. a) Schematic diagram of the device. b) Side view of the device, the fabrication material of each element is denoted, respectively. c) The dependence between Fermi-level of single-layer graphene and applied gate voltage under the parallel-plate capacitor model with different dielectric thickness. d) The absorptance map of single-layer graphene versus Fermi-level (E_F) and optical wavelength, transversals of common infrared wavebands are denoted as white dashed lines. e) Modulation depth (MD) for single-layer graphene transmittance (T) and FG-FETM reflectance (R) under common infrared wavelengths when Fermi-level gets tuned.

where $\alpha = \sigma/(\pi\epsilon_0 c_0)$, σ is the conductance of graphene, and c_0 is the light speed in vacuum. The detailed derivation can be found in the Supporting Information, S1. For single-layer graphene, the conductance can be derived from Kubo formula^[33–35]

$$\begin{aligned}\sigma &= \sigma_{\text{intra}} + \sigma_{\text{inter}} \\ \sigma_{\text{intra}} &= \frac{e^2}{h} \frac{|E_F|}{\pi} \frac{1}{\hbar\tau_1 - i\hbar\omega} \\ \sigma_{\text{inter}} &= \frac{e^2}{4\hbar} \left[1 + \frac{1}{\pi} \arctan \frac{\hbar\omega - 2|E_F|}{\hbar\tau_2} - \frac{1}{\pi} \arctan \frac{\hbar\omega + 2|E_F|}{\hbar\tau_2} \right. \\ &\quad \left. - \frac{i}{2\pi} \ln \frac{(2|E_F| + \hbar\omega)^2 + \hbar^2\tau_2^2}{(2|E_F| - \hbar\omega)^2 + \hbar^2\tau_2^2} \right] \quad (3)\end{aligned}$$

where ω is the angular frequency of incident light, τ_1 is the intraband transition relaxation rate, and τ_2 is the interband transition relaxation rate. For graphene, the reflectance is negligible ($<0.1\%$), thus the absorptance $A \approx 1 - T$. Through numerical calculation, the map of absorptance depending on Fermi-level and light wavelength is depicted in Figure 1d. The absorption is finely tuned when Fermi-level shifts from 0 to 0.5 eV across the near- to mid-infrared wavebands owing to the universal absorption of graphene. In particular, four common wavebands in application, 1.00, 1.31, 1.55, and 2.00 μm , are intercepted for investigation. Considering the multilayer reflecting scheme, the global reflectance of FG-FETM can be expressed as

$$R = T_1^2 R_M T_G^2 \quad (4)$$

where T_1 is the transmittance of $\text{SiO}_2\text{--Al}_2\text{O}_3$ interface ($\approx 99.3\%$), R_M is the reflectance of mirror (near 100% for Cr/Au), and T_G is the transmittance of single-layer graphene which plays the dominant role in the modulation process. Figure 1e plots the transmittance of single-layer graphene and reflectance of the FG-FETM scheme tuned by Fermi-level within 0.5 eV scale under the four wavelengths. With slowly rise at first, rapidly increase around $\hbar\omega$ and thereafter saturation, the tuning trend shows nonlinearity but stays monotonic. Also as denoted in the plots, modulation depth can be nearly doubled by adopting a reflecting configuration compared with pure transmission.

3. Fabrication Methods

Although graphene exfoliated from bulk usually has better quality and well-ordered crystal structure, the micrometer-scale lateral size and random thickness of graphene flake make it difficult to locate and determine layer number, hindering standard device fabrication workflow with uniform structure. Thus, graphene developed by chemical vapor deposition (CVD) technique is adopted for the FG-FETM fabricating. **Figure 2a** illustrates the sequential fabrication workflow of the FG-FETM device: 1) The commercially available CVD synthesized graphene films on polycrystalline Cu substrate are firstly spin-coated with a layer of polymethyl methacrylate (PMMA), then the original Cu substrate is etched for a PMMA-supported film. 2) The standard single-mode fiber (SMF-28e) is fixed in a ceramic ferrule and polished to obtain smooth end-face, then the facet gets spin-coated with EBL resist. After

patterned electron beam exposure and development, the end-face is deposited with Au by electron beam evaporation (EBE). By removing extra resists, the dual electrodes are completed. Details of fiber-tip spin-coating and EBL techniques are introduced in the Supporting Information, S2. 3) PMMA-coated graphene in Step 1 is transferred onto the end-face and baked at 120 $^\circ\text{C}$ for 20 min to enhance the adhesion to end-face substrate, then the PMMA is removed by acetone. Next, the facet is spin-coated with resists again for second EBL patterning, and a rectangular area that covers fiber core and tips of electrodes remains after development. The other exposed parts of graphene are removed by plasma etching, and the portion of patterned graphene is obtained after dissolving resists. 4) The EBL processing for patterned area of dielectric is performed, which is similar to Step 2, and Al_2O_3 is deposited through EBE. 5) The EBL processing for patterned area of top-gate is performed, and Cr is deposited before Au to improve the adhesion with Al_2O_3 layer during EBE procedure. After removal of final resists, the FG-FETM device is accomplished.

As key intermediate phases of the FG-FETM fabrication process, Figure 2b shows dual electrodes completed in Step 2 while patterned graphene film in Step 3 is presented in Figure 2c. The dimension of graphene is $35 \times 15 \mu\text{m}^2$ and the channel width between dual electrodes is about 23 μm . A demonstrative picture of an accomplished sample and the corresponding microscopic photo are shown in Figure 2d. The dielectric region takes on rectangular geometry of $80 \times 60 \mu\text{m}^2$ to cover graphene and source–drain pair. On top of the dielectric there lays gate-electrode/reflecting mirror with width of $\approx 20 \mu\text{m}$, which exactly covers the fiber core and avoids overlapping directly above source/drain electrodes to prevent breakdown of dielectric. Larger pads extending from fiber-end-face electrodes to ceramic ferrule facet are also designed and fabricated for contacting and driving of electric probes, shown in **Figure 3d–i**.

4. Results and Discussion

The gate-tunable modulator based on single-layer graphene was firstly investigated. Shown in Figure 3a, Raman spectrum of employed single-layer graphene was measured by 488 nm laser source and a 100 \times objective lens, where three peaks: D, G, and 2D bands are situated at 1352.48, 1583.21, and 2691.88 cm^{-1} , respectively. The strong 2D peak with narrow Lorentz profile and relatively weak D peak indicate that the graphene is monolayer. The peak intensity ratio of the 2D band to the G band was ≈ 3.2 while that of the D band to the G band is less than 0.23, implying fewer defects and better graphene quality.^[36]

The reflecting scheme shall enable the formation of standing wave around the fiber end-face, and meanwhile considering the relatively weak absorption of single-layer graphene, it is feasible to design the thickness of dielectric so that the graphene can be located at antinode region for higher modulation. As plotted in Figure 3b, the standing wave field distribution was simulated through finite-element analysis, where the wavelength was set as 1550 nm, and refractive index adopted were 1.4682 for SMF-28e core, 1.7462 for Al_2O_3 dielectric, and $0.558 + 10.756i$ for Au. Thereby, the thickness of Al_2O_3 dielectric was determined as 225 nm for single-layer graphene. Figure 3c shows the sectional

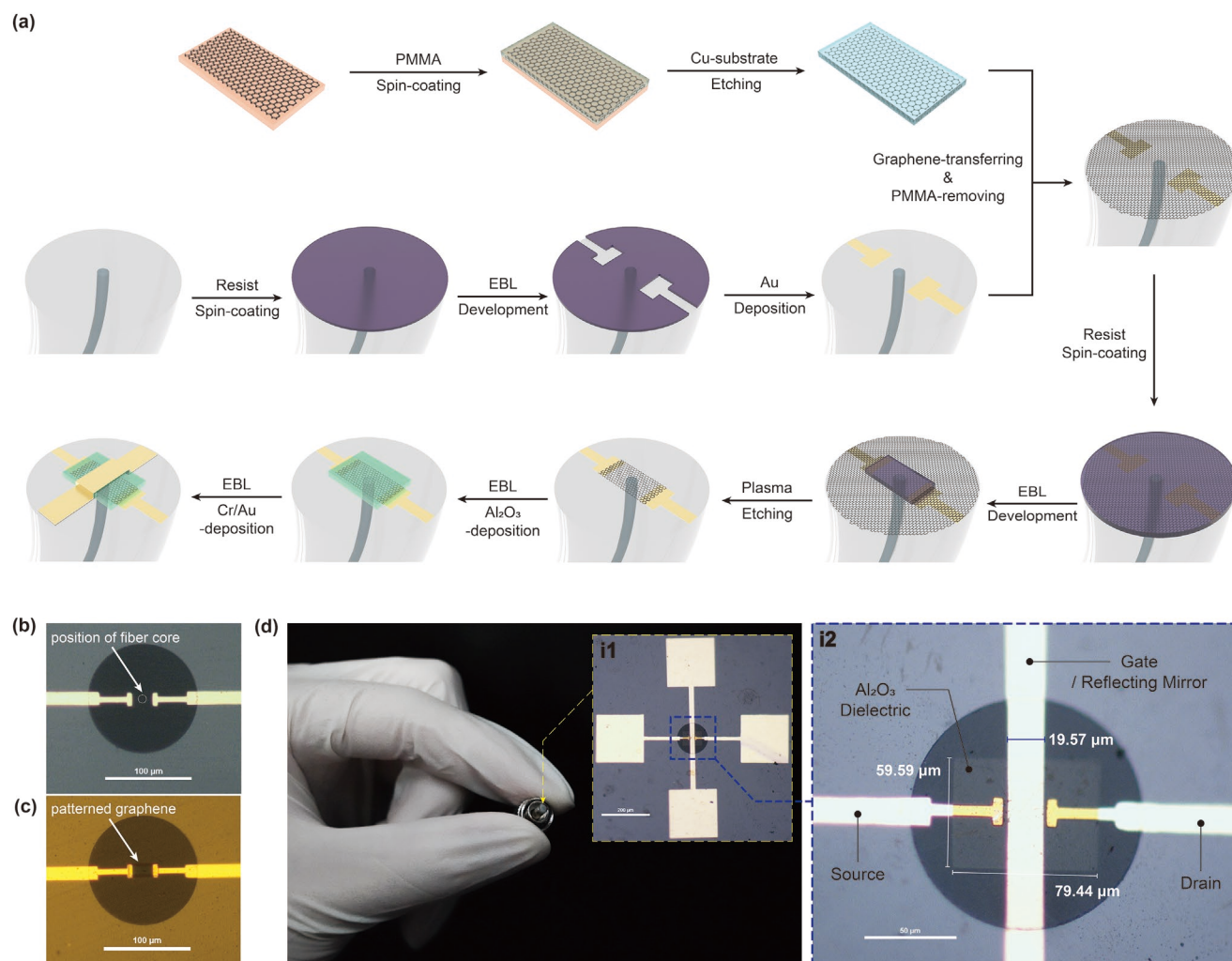


Figure 2. Fabrication of FG-FETM. a) Sequential fabrication workflow of FG-FETM. Microscopic photos of b) patterned end-face dual electrodes and c) patterned graphene film, both scale bars are 100 μm . d) The completed FG-FETM sample, where insets (i1) and (i2) show the enlarged microscopic photos of fiber-end-face. The scale bars represent 200 μm for (i1) and 50 μm for (i2), respectively.

scanning electron microscope (SEM) photo of FG-FETM based on the design, where the real thickness of Al_2O_3 in fabrication was 234.5 nm by measurement.

The device is characterized through experimental setups illustrated in **Figure 4a**. A 1550 nm single-wavelength high-stable continuous-wave (CW) laser works as optical source.

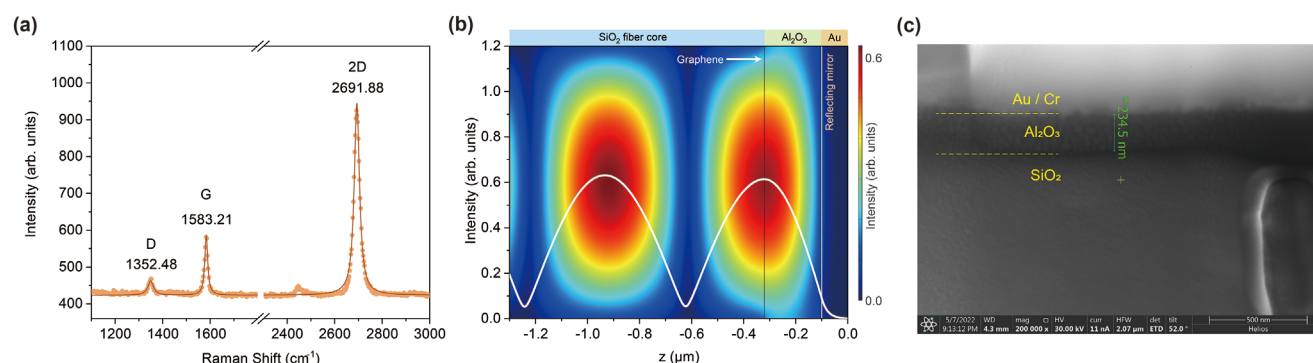


Figure 3. Single-layer graphene-based FG-FETM. a) Raman spectrum of employed single-layer graphene. b) Standing wave distribution of reflecting region, different areas of material are noted on the top, and the white curve represents normalized intensity along light propagating direction (z -direction) on the central axis. c) SEM sectional view of single-layer graphene-based FG-FETM.

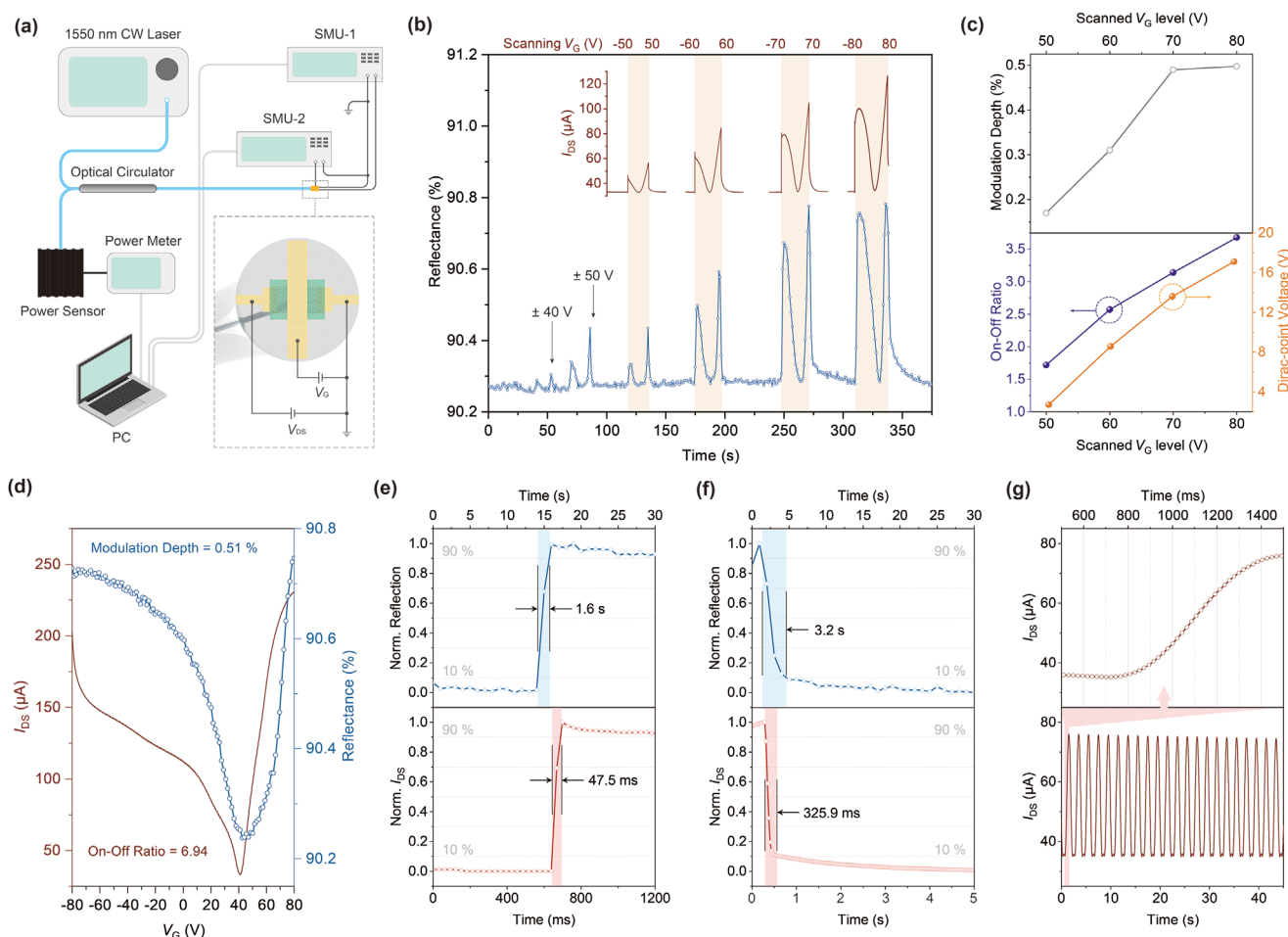


Figure 4. Characterization of single-layer graphene-based FG-FETM. a) Experimental setup of electro-optical modulation measurement, SMU, source-meter unit. Inset plot in dashed line box shows the circuit connection of three electrodes. b) Continuous tunability of device reflectance with gate voltage scanning from ± 50 to ± 80 V, synchronal drain-source current tuning curves are plotted in redline. c) Modulation depth, on-off ratio, and Dirac-point voltage varied with scanned gate voltage level. d) The maximum modulation depth achieved by single-layer graphene-based FG-FETM in blue dotted line, with corresponding drain-source current curve in redline. e) Optically (blue) and electrically (red) rise time, and f) optically (blue) and electrically (red) fall time for the device. g) Drain-source current response to sinusoidal gate voltage.

Light emitted from CW laser goes through an optical circulator and get reflected at FG-FETM, the modulated light passes circulator again and gets collected by optical power sensor (Thorlabs S145C) that connected to power meter (Thorlabs PM100D). Meanwhile, two source-meter unit (SMU) are used to apply drain-source voltage (V_{DS}) and gate voltage (V_G) as well as to measure current at the same time. As shown in dashed box inset in Figure 4a, SMU-1 (Keithley 2450) is connected to dual electrodes through probes to apply V_{DS} , and SMU-2 (Keithley 2400) is connected to top electrode to apply V_G , with two SMUs sharing same ground terminal. Furthermore, the two SMUs and power meter are all connected to PC for synchronized control and measurement.

The V_{DS} was fixed at 100 mV, and power meter started logging before application of V_G , as shown in Figure 4b. The original global reflectance of the device was 90.27%, with 33.2 μ A drain-source current (I_{DS}), corresponding to resistance of 3.01 k Ω . Then V_G was scanned symmetrically from negative to positive. The observable reflectance modulation starts when

scanning V_G reached the level of ± 40 V and became quantifiable at ± 50 V. Figure 4b labels the continuous tuning of reflectance with scanning V_G from ± 50 to ± 80 V in pale-orange ribbon, with synchronal I_{DS} monitoring curves above. Significant parameters during scanning V_G modulation are investigated and plotted in Figure 4c for reference. It can be seen from the gray curve that modulation depth of reflectance grows with scanned V_G level but turned saturated over ± 70 V, indicating the Fermi-level has been pushed to critical condition while the modulation depth do not meet simulation due to intrinsic loss of the device fabrication. Meanwhile, the electrical on-off ratio and Dirac-point voltage exhibits linear increasing, showing p-doped process. Figure 4d plots the maximum modulation depth achieved by single-layer graphene-based FG-FETM. Reflectance was monotonically controlled by V_G on both sides of Dirac point, and the optical modulation depth reached 0.51% along with the largest electrical on-off ratio of 6.94 in experiment. The Dirac-point voltage located at 40.84 V, exhibiting p-doped feature. The I_{DS} - V_G curve in Figure 4d shows asymmetrical profile

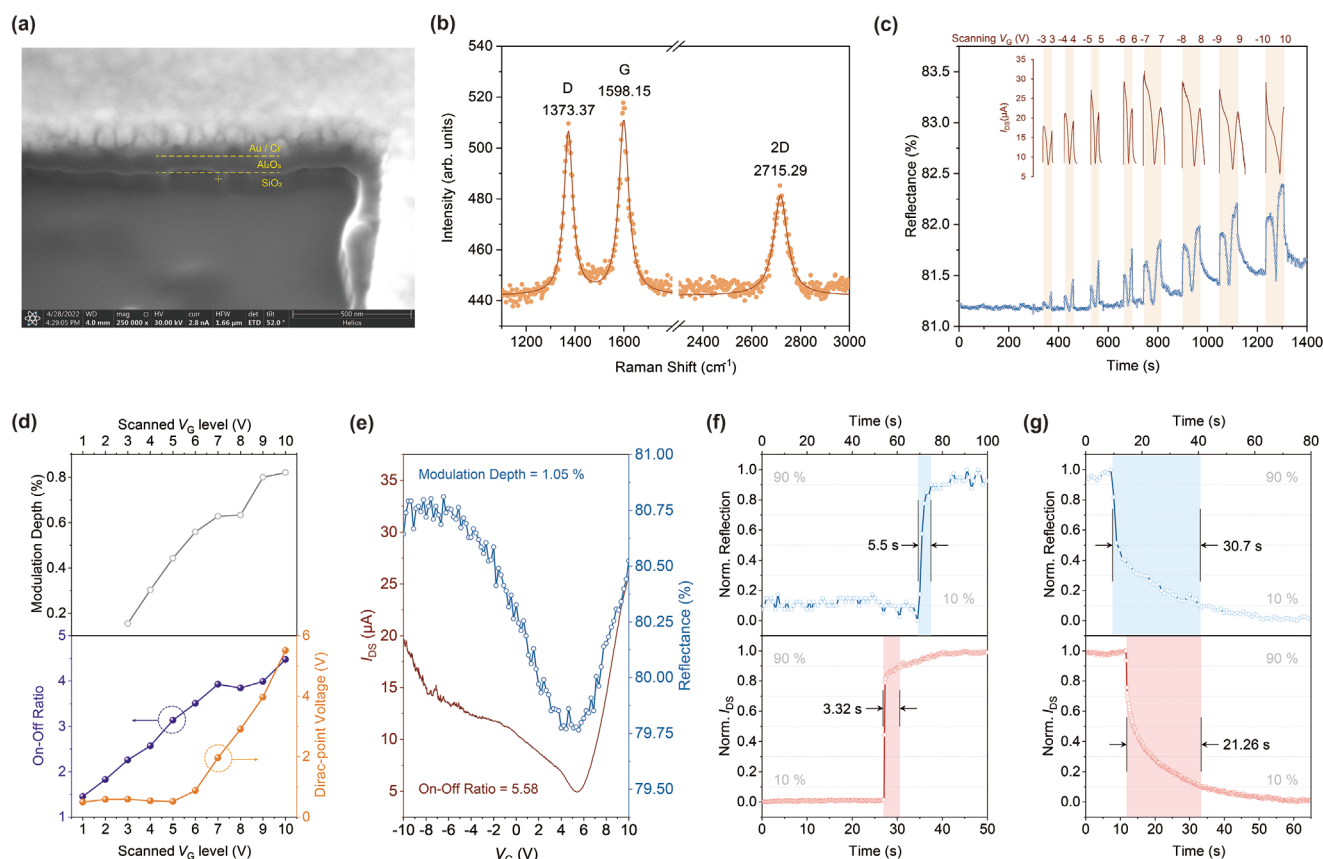


Figure 5. Characterization of few-layer graphene-based FG-FETM. a) SEM sectional view of few-layer graphene-based FG-FETM. b) Raman spectrum of employed few-layer graphene. c) Continuous tunability of device reflectance with gate voltage scanning from ± 3 to ± 10 V, synchronal drain–source current tuning curves are plotted in redline. d) Modulation depth, on-off ratio, and Dirac-point voltage varied with scanned gate voltage level. e) The maximum modulation depth achieved by few-layer graphene-based FG-FETM in blue dotted line, with corresponding drain–source current curve in redline. f) Optically (blue) and electrically (red) rise time, and g) optically (blue) and electrically (red) fall time for the device.

with Schottky junction at negative V_G area, which indicates the non-ohmic contacts between graphene and electrode. During the process of graphene etching, the chemical properties of resist polymer can be changed by oxygen plasma, subsequently hindering fully removal by acetone. The remains at graphene surface result in the non-ohmic contacts and unwanted doping. The nonideal interfacial contact is expected to be suppressed with optimization of etching power, time, and oxygen flow in etching and developing process.

Responses to dynamic manipulation were also measured. Step-response rise and fall time of optical and electrical on-off manipulation were investigated, depicted in Figure 4e,f. The I_{DS} response in red plot shows 475 and 325.9 ms for 10%–90% rise/fall time, respectively, while corresponding reflectance rises at 1.6 s and falls at 3.2 s, exhibiting hysteresis. H_2O/O_2 molecules absorbed by Si–OH bonds on silica fiber facet are responsible for the slow electrical control, which is interpreted in detail in the Supporting Information, S3. In addition, for top-gated graphene-based devices, EBE deposition method may cause defects in graphene film and degradation of carrier mobility.^[37] The FG-FETM's dynamic performance is believed to be enhanced through optimizing graphene transferring process, adding hydrophobic buffer layer that avoids H_2O/O_2 absorbates accumulation at substrate surface, and adopting sophisticated

dielectric material film growth technique like atom layer deposition which features denser film quality. Nonetheless, the device with long recovery time could still be useful in optical-fiber-based nonvolatile transistor and memory or precise optical interface modulation.^[38] A 0.25 Hz sinusoidal pulse train generated from signal generator was also applied to the gate electrode, and the I_{DS} shows agile response with continuity (Figure 4g).

To achieve higher tuning range, FG-FETM based on few-layer graphene was then investigated. The employed graphene was also grown through CVD methods on polycrystalline Cu substrate, with layer number ranging within 3–5. Allowing for the relatively thicker light interaction length and aiming to reduce gate voltage level for efficiency, thickness of dielectric was decreased to 30 nm in design, as shown in Figure 5a. Raman spectrum of employed graphene in Figure 5b displays D, G, and 2D bands at 1373.37, 1598.15, and 2715.29 cm^{-1} , respectively. The high G band and weak 2D band indicate few-layer properties. Typically, the G band of undoped CVD-grown few-layer graphene on Cu-substrate locates around 1580 cm^{-1} .^[39] Here, the measured G peak with shift of 18.15 cm^{-1} demonstrates a heavily doping phase. The peak intensity ratio of D band to G band reaches 0.89, implying slightly more defects which could be avoided via optimization of rinsing, annealing, and etching techniques in fabrication stage.

In Figure 5c, continuous tuning was performed, where the sample reflectance without V_G was 81.17%, with I_{DS} of 8.1 μ A corresponding to resistance of 12.3 k Ω . Observable modulation began at V_G level of ± 3 V, followed by scanning V_G from ± 4 to ± 10 V labeled with corresponding I_{DS} curves above. From Figure 5d it can be seen that the modulation depth of reflectance grows nearly proportional to scanned V_G level and saturates over ± 8 V. The electrical on-off ratio exhibits analogous trend of increasing and saturating in purple curve. The Dirac-point voltage keeps at a low level around 0.52 V at first, showing slightly p-doped of few-layer graphene, but increases proportionally when scanned V_G level climbs over ± 6 V, which resembles the doping process in single-layer graphene devices.

Figure 5e demonstrates the largest tuning scale based on few-layer graphene FG-FETM samples, which achieved reflectance modulation depth of 1.05% and electrical on-off ratio of 5.58. The gate-manipulating range was approximately doubled compared to single-layer graphene device. Furthermore, the dynamic switching properties were investigated and presented in Figure 5f for rise and Figure 5g for fall. The I_{DS} response in red takes on rise time of 3.32 s and fall time of 21.26 s, with corresponding reflectance in blue rises at 5.5 s and falls at 30.7 s, which are much slower than single-layer graphene counterparts in previous demonstration. Apart from absorbates at SiO₂-graphene interface noted earlier, multilayer stacking also limits the responding and recovering rate. And structurally, reduced thickness of dielectric greatly increases the device capacitance, thus lengthening the response time in rise and fall (see the Supporting Information, S3). Hence, a trade-off between achieving high speed and gating efficiency should be balanced in further design of FG-FETM.

5. Conclusion

In summary, a gate-tunable graphene electro-optical modulator directly fabricated on fiber tip is proposed and demonstrated, along with the fiber-end-face FET fabrication methods. The device makes features of all-fiber reflecting-mirror configuration and compactness of packaging, obtains reflectance modulation depth over 0.5% for single-layer graphene sample and 1% for few-layer graphene sample in demonstration, verifying the feasibility of such design and fabrication technique. The device is believed to see prospective application in tuning of minor-scale fiber lasers or fiber resonators, and the fabrication flows are universal to extensive ranges of 2D materials, expanding the scenario of "lab on fiber" concept.

Supporting Information

Supporting Information is available from the Wiley Online Library or from the author.

Acknowledgements

This work was supported by National Natural Science Foundation of China (62135007 and 61925502). The authors thank Prof. Yufeng Hao and Mr. Yushu Wang for help in Raman characterization.

Conflict of Interest

The authors declare no conflict of interest.

Data Availability Statement

The data that support the findings of this study are available from the corresponding author upon reasonable request.

Keywords

electro-optical modulator, fiber devices, field-effect transistors, graphene

Received: August 22, 2022

Revised: September 5, 2022

Published online: September 22, 2022

- [1] K. S. Novoselov, A. K. Geim, S. V. Morozov, D. Jiang, Y. Zhang, S. V. Dubonos, I. V. Grigorieva, A. A. Firsov, *Science* **2004**, 306, 666.
- [2] A. Krasnok, S. Lepeshov, A. Alu, *Opt. Express* **2018**, 26, 15972.
- [3] Y. Zhang, Y. Zheng, K. Rui, H. H. Hng, K. Hippalgaonkar, J. Xu, W. Sun, J. Zhu, Q. Yan, W. Huang, *Small* **2017**, 13, 1700661.
- [4] X. Guo, W. Wang, H. Nan, Y. Yu, J. Jiang, W. Zhao, J. Li, Z. Zafar, N. Xiang, Z. Ni, W. Hu, Y. You, Z. Ni, *Optica* **2016**, 3, 1066.
- [5] Q. Bao, H. Zhang, B. Wang, Z. Ni, C. H. Y. X. Lim, Y. Wang, D. Y. Tang, K. P. Loh, *Nat. Photonics* **2011**, 5, 411.
- [6] Y. Zhao, X.-G. Li, X. Zhou, Y.-N. Zhang, *Sens. Actuators, B* **2016**, 231, 324.
- [7] C. T. Phare, Y.-H. D. Lee, J. Cardenas, M. Lipson, *Nat. Photonics* **2015**, 9, 511.
- [8] J. Yan, Y. Zhang, P. Kim, A. Pinczuk, *Phys. Rev. Lett.* **2007**, 98, 166802.
- [9] J. Kim, H. Son, D. J. Cho, B. Geng, W. Regan, S. Shi, K. Kim, A. Zettl, Y. R. Shen, F. Wang, *Nano Lett.* **2012**, 12, 5598.
- [10] L. Ren, Q. Zhang, J. Yao, Z. Sun, R. Kaneko, Z. Yan, S. Nanot, Z. Jin, I. Kawayama, M. Tonouchi, J. M. Tour, J. Kono, *Nano Lett.* **2012**, 12, 3711.
- [11] E. J. Lee, S. Y. Choi, H. Jeong, N. H. Park, W. Yim, M. H. Kim, J. K. Park, S. Son, S. Bae, S. J. Kim, K. Lee, Y. H. Ahn, K. J. Ahn, B. H. Hong, J. Y. Park, F. Rotermund, D. I. Yeom, *Nat. Commun.* **2015**, 6, 6851.
- [12] C. Li, J. Chen, W. Wang, T. Wang, S. Yan, D. Li, F. Xu, C. Mou, Y. Lu, *Adv. Opt. Mater.* **2017**, 5, 1700630.
- [13] J.-H. Chen, B.-C. Zheng, G.-H. Shao, S.-J. Ge, F. Xu, Y.-Q. Lu, *Light: Sci. Appl.* **2015**, 4, e360.
- [14] M. Liu, X. Yin, E. Ulin-Avila, B. Geng, T. Zentgraf, L. Ju, F. Wang, X. Zhang, *Nature* **2011**, 474, 64.
- [15] S. J. Koester, H. Li, M. Li, *Opt. Express* **2012**, 20, 20330.
- [16] B. Yao, S. W. Huang, Y. Liu, A. K. Vinod, C. Choi, M. Hoff, Y. Li, M. Yu, Z. Feng, D. L. Kwong, Y. Huang, Y. Rao, X. Duan, C. W. Wong, *Nature* **2018**, 558, 410.
- [17] J.-H. Chen, D.-R. Li, F. Xu, *J. Lightwave Technol.* **2019**, 37, 2577.
- [18] K. Xu, Y. Xie, H. Xie, Y. Liu, Y. Yao, J. Du, Z. He, Q. Song, *J. Lightwave Technol.* **2018**, 36, 4730.
- [19] M. K. Shah, S.-W. Ye, X.-H. Zou, F. Yuan, A. Jha, Y. L. Zhang, R.-G. Lu, Y. Liu, *IEEE J. Sel. Top. Quantum Electron.* **2017**, 23, 89.
- [20] N. An, T. Tan, Z. Peng, C. Qin, Z. Yuan, L. Bi, C. Liao, Y. Wang, Y. Rao, G. Soavi, B. Yao, *Nano Lett.* **2020**, 20, 6473.
- [21] Y. Li, N. An, Z. Lu, Y. Wang, B. Chang, T. Tan, X. Guo, X. Xu, J. He, H. Xia, Z. Wu, Y. Su, Y. Liu, Y. Rao, G. Soavi, B. Yao, *Nat. Commun.* **2022**, 13, 3138.

- [22] N. H. Park, S. Ha, K. Chae, J.-Y. Park, D.-I. Yeom, *Nanophotonics* **2020**, 9, 4539.
- [23] Z. Xiao, K. Wu, T. Li, J. Chen, *Opt. Express* **2020**, 28, 14933.
- [24] C. Qin, K. Jia, Q. Li, T. Tan, X. Wang, Y. Guo, S. W. Huang, Y. Liu, S. Zhu, Z. Xie, Y. Rao, B. Yao, *Light: Sci. Appl.* **2020**, 9, 185.
- [25] D. Li, H. Xue, M. Qi, Y. Wang, S. Aksimsek, N. Chekurov, W. Kim, C. Li, J. Riikonen, F. Ye, Q. Dai, Z. Ren, J. Bai, T. Hasan, H. Lipsanen, Z. Sun, *2D Mater.* **2017**, 4, 025095.
- [26] J. Bogusławski, Y. Wang, H. Xue, X. Yang, D. Mao, X. Gan, Z. Ren, J. Zhao, Q. Dai, G. Soborń, J. Sotor, Z. Sun, *Adv. Funct. Mater.* **2018**, 28, 1801539.
- [27] D. Li, H. Xue, Y. Wang, M. Qi, W. Kim, C. Li, J. Riikonen, Z. Ren, J. Bai, H. Lipsanen, Z. Sun, *Opt. Lett.* **2018**, 43, 3497.
- [28] K. Y. Lau, A. P. Perros, D. Li, M. Kim, Z. Sun, *Nanoscale* **2021**, 13, 9873.
- [29] F. Wang, Y. Zhang, C. Tian, C. Girit, A. Zettl, M. Crommie, Y. R. Shen, *Science* **2008**, 320, 206.
- [30] A. B. Kuzmenko, E. van Heumen, F. Carbone, D. van der Marel, *Phys. Rev. Lett.* **2008**, 100, 117401.
- [31] R. R. Nair, P. Blake, A. N. Grigorenko, K. S. Novoselov, T. J. Booth, T. Stauber, N. M. Peres, A. K. Geim, *Science* **2008**, 320, 1308.
- [32] A. Armano, S. Agnello, *C* **2019**, 5, 67.
- [33] G. W. Hanson, *J. Appl. Phys.* **2008**, 103, 064302.
- [34] Q. Bao, K. P. Loh, *ACS Nano* **2012**, 6, 3677.
- [35] S. A. Mikhailov, K. Ziegler, *Phys. Rev. Lett.* **2007**, 99, 016803.
- [36] M. Huang, P. V. Bakharev, Z. J. Wang, M. Biswal, Z. Yang, S. Jin, B. Wang, H. J. Park, Y. Li, D. Qu, Y. Kwon, X. Chen, S. H. Lee, M. G. Willinger, W. J. Yoo, Z. Lee, R. S. Ruoff, *Nat. Nanotechnol.* **2020**, 15, 289.
- [37] Z. H. Ni, H. M. Wang, Y. Ma, J. Kasim, Y. H. Wu, Z. X. Shen, *ACS Nano* **2008**, 2, 1033.
- [38] J. T. Kim, H. Choi, Y. Choi, J. H. Cho, *ACS Appl. Mater. Interfaces* **2018**, 10, 1836.
- [39] A. Kumar, A. A. Voevodin, D. Zemlyanov, D. N. Zakharov, T. S. Fisher, *Carbon* **2012**, 50, 1546.